

# Characterization of a Friction Stir Weld in Aluminum Alloy 7055 Using Microhardness, Electrical Conductivity, and Differential Scanning Calorimetry (DSC)



RALPH BUSH, MICHELLE KIYOTA, and CATHERINE KIYOTA

Optical microscopy, microhardness, electrical conductivity, and differential scanning calorimetry (DSC) were used to characterize the microstructure, hardness, and precipitate structure as a function of position in a friction stir weld, naturally aged for 10 years, in aluminum alloy 7055. Results are shown for the as-welded/naturally aged condition and for a weld that was post-aged using a  $-T76$  regimen. The grain structure and microhardness results reveal the expected central recrystallized region, a thermo-mechanical affected zone (TMAZ), and heat-affected zone (HAZ) with typical changes in microhardness. DSC scans for the as-welded/naturally aged condition indicate a precipitate structure similar to that of a naturally aged condition in the central recrystallized region. Maximum precipitate coarsening and overaging occurs near the TMAZ/HAZ boundary with reduced precipitate dissolution and coarsening as the distance from the weld increases. The post-weld aging resulted in the transformation of GP zones to more stable precipitates plus coarsening of the more stable  $\eta'$  and  $\eta$  precipitates. A combination of DSC testing and CALPHAD calculations allowed calculation of precipitate volume fraction in the HAZ. The precipitate volume fraction decreased monotonically from 0.052 in the baseline material to 0.044 at the TMAZ/HAZ interface.

DOI: 10.1007/s11661-016-3506-7

© The Minerals, Metals & Materials Society and ASM International (outside the USA) 2016

## I. INTRODUCTION

FRICITION stir welding is a solid-state welding process developed by the Welding Institute in the UK.<sup>[1,2]</sup> The process involves insertion of a spinning tool into the intended weld joint to create heat *via* friction and associated plastic deformation. The tool is passed along the joint causing the metal from each side of the joint to flow in a circular fashion into the mating side. The process can be used to create high quality joints that are free from defects typically associated with fusion-welded joints, such as hydrogen porosity and hot-cracking. This is particularly useful for highly alloyed aerospace aluminum alloys in the 2XXX and 7XXX alloy families, which are normally considered unweldable by conventional fusion welding methods.<sup>[3]</sup>

During friction stir welding the material experiences high temperatures and plastic deformation for short durations. The material behavior under these thermo-mechanical conditions, including precipitate behavior, is not fully understood. Dissolution, coarsening, and re-precipitation behavior of precipitates during welding is critical

for understanding the mechanical strength and corrosion performance of these welds. Thus, quantitative characterization of precipitates is paramount.

The microstructure in and around a friction stir weld can be placed into three categories, specifically, the thermo-mechanical affected zone (TMAZ), heat-affected zone (HAZ), and unaffected zone or parent material. In aluminum alloys, the TMAZ consists of a central nugget which consists of small, recrystallized grains. This region is found in the material through which the rotating pin traveled and extends a slight distance beyond. Further out from the weld center, the TMAZ microstructure consists of grains deformed by plastic flow of the welding process. The grain structure of the HAZ is similar to that of the parent material, but can sometimes be distinguished by a differing response to etching.<sup>[4]</sup>

Microhardness profiles in 7XXX alloy friction stir welds can exhibit either a W or U-shape depending on the peak temperature reached during welding. Reported peak temperatures range from 573 K to 773 K (300 °C to 500 °C). A U-shaped profile typically results when the peak temperature is on the order of 573 K to 623 K (300 °C to 350 °C), whereas the W-shape results when the peak temperature in the nugget region is slightly below or above the precipitate solvus. For the W-shaped profiles, the central nugget region exhibits a greater hardness than the surrounding TMAZ. Reported peak temperatures in this region are on the order of 723 K to 773 K (450 °C to 500 °C), when W-shaped profiles are observed. The result is dissolution of the precipitates, a

RALPH BUSH, Associate Professor, is with the Department of Engineering Mechanics, US Air Force Academy, USAF Academy, CO 80840. Contact e-mail: ralph.bush@usafa.edu MICHELLE KIYOTA and CATHERINE KIYOTA, First Lieutenants, are with the Department of Chemistry, US Air Force Academy, USAF Academy.

Manuscript submitted December 22, 2015.

U.S. Government Work. Not Protected by U.S. Copyright.

Article published online April 13, 2016

supersaturated solution, followed by limited grain boundary re-precipitation and natural aging. The hardness of the nugget increases with time as the natural aging process progresses. The peak welding temperature in the surrounding TMAZ is below the precipitate solvus. This produces dissolution of smaller precipitates and coarsening of larger ones with little supersaturation, resulting in a hardness decrease. The hardness minimum generally occurs at the location where the peak welding temperature is about 623 K (350 °C). The hardness gradually increases throughout the HAZ until it reaches the hardness of the parent material. This observation is attributed to lower temperatures encountered in this region during welding and less subsequent precipitate dissolution and coarsening.<sup>[4-15]</sup>

Characterization of the precipitate structure within a friction stir weld and its vicinity has been performed with a variety of methods, including differential scanning calorimetry (DSC), transmission electron microscopy (TEM), and small angle X-ray analysis (SAXS). DSC is the least expensive of the three methods. DSC requires less time for data acquisition and data analysis, as well as less technical expertise than the other two methods. It can reproducibly and accurately measure the temperatures at which precipitate dissolution and formation reactions occur. Measurement of these temperatures can be used to identify the precipitate reaction that occurs at the temperature in question. Small changes in the reaction temperature and peak broadening can be used as an indication of precipitate coarsening during prior thermal processing. Proper measurement techniques can in some cases provide an approximate measure of the precipitate volume fraction and the activation energy of the precipitate transformation reaction. However, DSC must be supplemented with other methods to confirm the identity of the precipitate(s) participating in the reactions. Precipitate identity is generally implied by use of precipitate progression knowledge of a particular alloy along with TEM or SAXS work done previously or in conjunction with the DSC analysis. Once the supplemental TEM or SAXS work is completed for a given alloy system, it need not be redone each time. TEM can be used to identify precipitates present at a given location of the weld, but does not easily provide quantitative information. SAXS can identify the precipitates present, provide quantitative information as a function of position, and can be performed *in situ*. However, it requires more expensive equipment, software, and a higher degree of technical expertise than DSC.<sup>[5,7-9,16-21,27]</sup>

Coupled with TEM, DSC has been successfully used to identify precipitates and track their dissolution and coarsening in a number of processes that involve thermal excursions, including aging,<sup>[22-34]</sup> overheating,<sup>[35]</sup> friction stir welding,<sup>[5,7,8]</sup> and retrogression and re-aging.<sup>[33,36,37]</sup> Study of the literature reveals many DSC scans of standard 2XXX and 7XXX aluminum alloys. The peaks have been correlated, by use of other means, with specific GP zone and precipitate dissolution and formation reactions. In many cases these scans may be used to aid in identification of the precipitate reaction associated with a given peak without the need for corroborating TEM work.

Previous studies have been conducted that use DSC to characterize friction stir welds in precipitation-strengthened aluminum alloys. DSC scans in the TMAZ and HAZ show reduced or non-existent GP dissolution peaks as compared to base material as well as smaller precipitate formation peaks. This implies that GP zones in these regions dissolve during welding and that there is less solute available during the DSC scan for precipitate formation. In the nugget region of peak-aged and overaged alloys a DSC scan generally shows an increase in the area of the GP zone dissolution peak, whereas in naturally aged alloys this peak is similar in size to that found in baseline material. The precipitate formation peaks are generally smaller in area and translated to higher temperatures.<sup>[5,7,8]</sup>

Based on the discussion above, it is apparent that characterization techniques, such as SAXS provide the most quantitative information about the precipitate size and volume fraction as a function of position within a friction stir weld. However, this technique is not as widely available as DSC and requires greater in-house technical expertise. The goal of the research presented in this paper is to determine the extent of quantitative information that can be generated regarding the precipitate microstructure using commonly available characterization techniques, such as DSC, electrical conductivity, and microhardness available in smaller labs.

## II. MATERIAL

The alloy/product studied was commercial high-strength 19.1-mm-thick 7055-T7751 aluminum alloy plate used for aerospace applications. It maintains moderate fracture toughness and corrosion properties. As with most highly alloyed 7XXX aluminum alloys, 7055 is considered very difficult to weld using typical fusion welding techniques, making this alloy a good candidate for joining with the friction stir weld process. The nominal composition of 7055 is Al-8.0Zn-2.3Cu-2.0Mg-0.16Zr (wt pct). Hardness of the parent plate was 190 HV. Friction stir welding was performed at the University of South Carolina using a tool rotation speed of 200 rpm, a tool translation speed of 76.2 mm/min, and with a z-axis force of 60.2 kN. The tool shoulder measured 31.8 mm in diameter and the tool pin was 12.7 mm in diameter. After welding the material was naturally aged at room temperature for 10 years (approximately  $3.2 \times 10^8$  seconds). After the natural aging, one section of the material was given a two-step post-weld aging treatment of 8 hr. at 394 K (121 °C), followed by 5 hours at 436 K (163 °C). A ramp rate of 20° K per hour was used between the two aging steps. This two-step aging treatment approximates a -T76 aging treatment that would be used to improve corrosion resistance in the HAZ of the weld.<sup>[5,6]</sup>

## III. PROCEDURES

### A. Microhardness

Microhardness scans were made to characterize the hardness as a function of location normal to the weld.

The hardness measurements were made at plate mid-thickness on both the advancing and retreating sides of the weld starting at the weld center and progressing into the unaffected parent material. Microhardness scans were measured using a Vickers scale and a 500 g load. Specimens were metallographically polished prior to hardness measurements. Hardness measurements were made at 0.5 mm increments.

### B. Optical Metallography

The grain structure in different sections of the weld was characterized by optical microscopy. A Keller's etch solution was utilized to reveal the grain structure. Photographs were taken in the central nugget, TMAZ, HAZ, and parent material regions.

### C. Differential Scanning Calorimetry

DSC was used to characterize the precipitate structure in the various areas of the weld. Cylinders, 4 mm in diameter and 76 mm in length, were machined from the plate mid-thickness normal to the weld plane. The cylinders were centered on the weld line and the weld line center was marked on the cylinders. The advancing and retreating sides of the weld were marked on each cylinder. All cylinders spanned the entire width of the weld. Individual DSC specimens were cut from the cylinder using a Buehler low-speed diamond saw at locations corresponding to significant regions in the weld, such as the weld nugget, the hardness minimum, several locations spaced within the HAZ and in the parent material. One DSC specimen from the parent material was solution heat treated at 748 K (475 °C) for 30 minutes, quenched and stored in a freezer at 258 K (−15 °C) until DSC characterization. This was done to document the precipitate formation exotherms which characterize the precipitation sequence in 7055 and compare them to DSC exotherms of scans found in the literature for commercial 7XXX alloys.

All DSC analysis was performed on a TA Instruments DSC 2910 Differential Scanning Calorimeter Q100 system. Round disks with masses between 30 and 40 mg were cut from the aluminum cylinders described above and cleaned with methanol before analysis. DSC analysis was made with a purge gas flow rate of 50 mL/min of N<sub>2</sub>. The specimens were first equilibrated at 243 K (−30 °C) then heated to 773 K (500 °C) at a ramp rate of 10° K/minute. The data were then analyzed using TA Universal Analyzer software. A DSC curve of 99.99 pct pure Al powder was used as a baseline and subtracted from all the DSC scans. Curves were then rotated and shifted to be superimposed onto one another.

### D. Electrical Conductivity

Electrical conductivity measurements were made at the mid-thickness of the plate at 1 mm intervals starting at the weld center. A 1" thick weld cross section was cut from the plate and machined on both sides to ensure flatness and that the sides were parallel. To make the measurements, the weld cross section was clamped onto

a milling machine table. The conductivity probe was rigidly attached to the spindle. The table was moved in 1 mm intervals and the probe lowered onto the specimen for each measurement. Measurement scans were taken three times to ensure repeatability.

The measurements were made using a Hocking AutoSigma 3000 electrical conductivity meter with a probe diameter of 12.7 mm using a signal frequency of 60 kHz. Due to the probe size, the spatial resolution of the measurements was coarser than the interval at which they were taken.

Electrical conductivity measurements were not made on the post-weld aged material. Only a small portion of the welded section was post-weld aged. This portion was consumed during the DSC specimen extraction process prior to making electrical conductivity measurements.

## IV. RESULTS

### A. Metallography

A series of optical metallographs document the microstructure from starting at the weld center and finishing with parent material. Figure 1 is a low magnification overview of the weld microstructure showing the central nugget stir zone surrounded by a thermo-mechanically affected zone (TMAZ) followed by the heat-affected zone (HAZ) and parent material as distance from the weld center increases. The observed microstructure is typical of that in aluminum friction stir welds.

Figure 2 illustrates the contrast between the pancake-shaped, unrecrystallized grain structure of the parent material with the mechanically stirred, equiaxed, recrystallized grain structure of the central nugget. The figure shows that the stirring refined the grain diameter to about an average diameter of 10 μm while breaking up the dark Fe-based constituent particles.

Figures 3 through 5 show the microstructure in the TMAZ as it transitions between the nugget and HAZ. Figure 3 shows the transition from a completely recrystallized grain structure at the nugget–TMAZ interface to a completely unrecrystallized grain structure at a distance of approximately 8.7 mm from the weld center and 2.3 mm from the nugget edge. Mechanical stirring during the weld in this region is indicated by the approximate 45° orientation of the unrecrystallized grains to the horizontal plane.

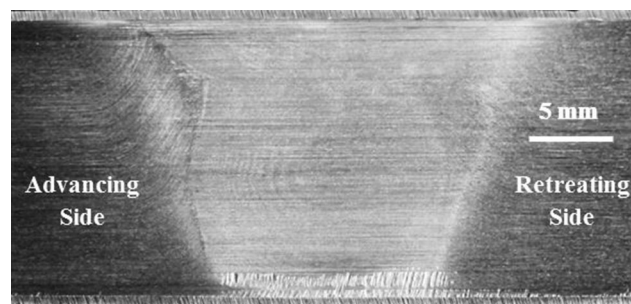


Fig. 1—Low magnification view of overall weld microstructure.

Figures 4 and 5 document the decreasing level of mechanical stirring and unrecrystallized grain structure as the HAZ is approached at 13 mm from the weld center. The grain structure in the HAZ is identical to that of the parent material in Figure 1. These microstructural features are typical of those observed in aluminum alloy friction stir welds.

### B. Hardness

Microhardness scans of the retreating sides of the naturally aged and post-weld artificially aged welds are

shown in Figure 6. Markers are also placed in this figure indicating the boundaries between the nugget, TMAZ, HAZ, and baseline regions. The hardness for both welds in the nugget averages approximately 170 HV. The hardness rises rapidly after crossing the nugget-TMAZ boundary and reaches a maximum between 180 and 190 HV at about 9.5 mm from the weld center. As the distance from the weld center increases in the TMAZ the hardness decreases rapidly and reaches a minimum at or near the TMAZ-HAZ boundary. This boundary occurs at approximately 13 mm from the weld center. The hardness monotonically

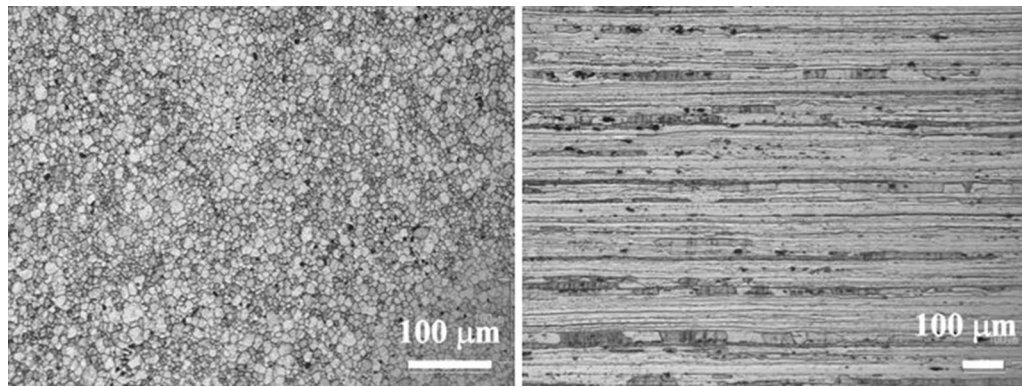


Fig. 2—Central nugget microstructure (left). Baseline parent material microstructure (right).

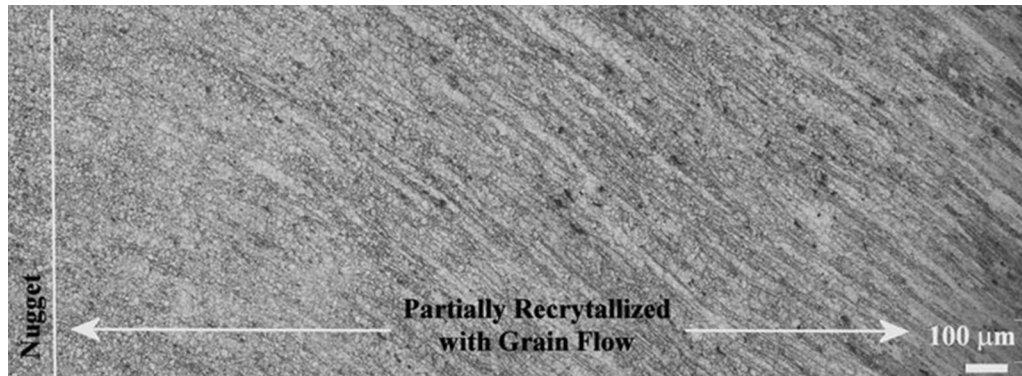


Fig. 3—Microstructure of TMAZ; 6.35 to 8.8 mm from weld center.

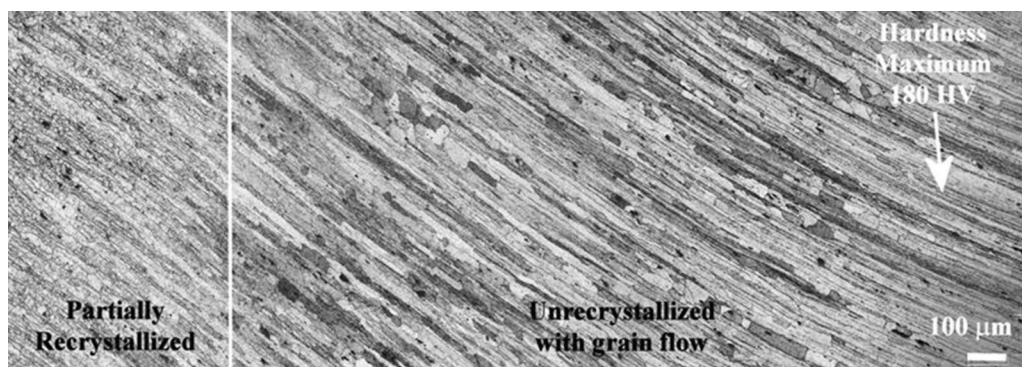


Fig. 4—Microstructure of TMAZ; 8.2 to 10.6 mm from weld center.

increases in the HAZ until the HAZ–baseline material boundary is reached at about 35 mm from the weld center. The hardness scans of the two aging conditions are similar in the nugget region and in the TMAZ up until 10.5 mm from the weld center. At distances between 10.5 and 25 mm the post-weld aged material is substantially less than that of the naturally aged material. At distances greater than 25 mm (half-way through the HAZ) the post-weld aged material hardness is approximately 10 HV less than that of the naturally aged material.

### C. Electrical Conductivity

Microhardness and electrical conductivity of the as-welded and naturally aged material are plotted in Figure 7 as a function of distance from weld center along with region boundary markers. Due to the large size of the conductivity probe compared to the fidelity of the spatial measurement interval, the conductivity values should be considered as a moving average. The electrical conductivity is constant in the nugget at a value consistent with a naturally aged, T3-type aging treatment and rises rapidly to a maximum shortly after crossing the TMAZ–HAZ boundary. The value at the maximum is consistent with the conductivity of an overaged T7-type aging treatment. The conductivity then decreases as it approaches that of the T77 baseline material.

The locations from which the DSC specimens were removed are also indicated on the microhardness scan of Figure 7. Locations were selected to be within the nugget, at/near the hardness minimum, half-way and 90 pct of the distance through the HAZ, and in the baseline material.

### D. DSC

A number of DSC scans were generated to document the change in precipitate structure and volume fraction as a function of position within the weld. The initial scan, shown in Figure 8, was of baseline material that had been re-solutionized at 748 K (475 °C) and held in a freezer at 258 K (−15 °C) until immediately prior the DSC scan. This scan illustrates the typical precipitation sequence in 7XXX aluminum alloys. Four significant peaks are labeled in this scan. A search of the literature found excellent and consistent agreement on the temperatures at which the peaks for each step in the precipitation sequence occurs.<sup>[22–37]</sup> All of these authors used TEM analysis to verify their DSC analysis. Thus, the precipitate transformation associated with each peak in the current work was identified based on comparison of the peak temperature with those identified in the literature, rather than separate TEM analysis. Peak I, centered at 363 K (90 °C), is associated with GP zone formation. Peak IIIb, centered at about 478 K (205 °C), is associated with  $\eta'$  precipitate formation. Peak IV is a doublet centered at 513 and 538 K (240 and 265 °C). These two peaks are generally ascribed to the formation and coarsening of  $\eta$  phase precipitates. Peak V, whose maximum occurs at approximately 693 K (420 °C), is

associated with dissolution of  $\eta$  phase precipitates. The DSC scan of Figure 8 is consistent with the precipitation sequence of



DSC scans for the baseline –T77 material and the two HAZ locations furthest from the weld center are shown in Figure 9. Peaks II, III, IV, and V are labeled in the Figure. Descriptions of the precipitation transformations occurring at each of these peaks is described in Table I. Table I also points out that multiple transformations are probably occurring simultaneously in the temperature regime between 473 K and 523 K (200 °C and 250 °C) rendering it difficult to quantify the amount of individual transformation product.

However, qualitative assessment of the curves is readily made. The baseline material scan consists of a broad endothermic dissolution peak, a combination of peak-types II and III, beginning below 373 K (100 °C) and ending around 393 K (220 °C). This is followed by an exothermic formation doublet, peak type IV, spanning from about 393 K to 543 K (220 °C to 270 °C). Followed by a broad endothermic dissolution peak that reaches its maximum heat flow between 673 K and 693 K (400 °C and 420 °C).

This analysis suggests that the precipitate structure of the baseline material consists primarily of a mixture of GP zones and  $\eta'$  precipitates, with a small amount of  $\eta$  precipitates. A T77 aging treatment consists of a low-high-low temperature regimen. The GP zones would result from the second low temperature aging step, whereas the  $\eta'$  and  $\eta$  precipitates would form during the first two aging steps. The presence of the first peak of the doublet in Peak IV indicates the transformation of  $\eta'$  precipitates to  $\eta$  precipitates during the scan. The second peak of the doublet indicates  $\eta$  precipitate coarsening during the DSC scan. As the location of the DSC scan within the HAZ approaches the weld center, the maximum temperature excursion during welding increases. As the weld center is approached in the HAZ it is observed that Peaks II and III become distinct from one another. The area under Peak II increases and the area under Peak III decreases. The area under Peak IVa decreases at 30 mm from the weld center without a concomitant decrease in the area under Peak IVb. This is consistent with a DSC scan for a 7XXX series aluminum alloy that has experienced further overaging. At a distance of 24 mm from the weld center, Peak IVa is absent, while the area under Peak IVb is significantly reduced compared to the baseline material. These observations indicate that some of the GP zones and smaller  $\eta'$  precipitates dissolve during welding, increasing the saturation level of the solute. During the natural aging period after welding, GP zones re-precipitate causing the increased area under Peak II. The temperature excursion during welding also causes some of the larger precipitates to transform from  $\eta'$  to  $\eta$  and then to rapidly coarsen or grow. This is manifested by the area decreases in Peaks III and IV as the location approaches the weld center.

DSC scans for material at the hardness minimum and central nugget are added to those from the HAZ and baseline in Figure 10. In both scans the GP zone dissolution peak, Peak II, increases rapidly with increasing maximum temperature during the welding. The  $\eta'$  dissolution peaks are missing indicating the lack of  $\eta'$  precipitates. The hardness minimum scan shows a larger and broader  $\eta'$  formation peak that appears to overlap the  $\eta$  formation peak. This scan also lacks a  $\eta$  precipitate coarsening peak. These results indicate that the thermal excursion resulted in significant dissolution of GP zones and smaller  $\eta'$  precipitates whose size was less than the critical particle size,  $r^*$ , of the thermal excursion, while transforming larger  $\eta'$  precipitates to  $\eta$  precipitates and coarsening them to a stable size that resist coarsening during the brief DSC scan. The precipitates that dissolved during welding then re-precipitated during natural aging to form the GP zones detected during the DSC scan.

Previous research has shown that temperatures in the nugget during friction stir welding exceed the solution heat treat temperature. This is consistent with the DSC scan in the nugget compared to that in Figure 8, as the

where  $f_v$  is the combined  $\eta'/\eta$  precipitate volume fraction at a specific location in the HAZ,  $f_{vb}$  is the combined  $\eta'/\eta$  precipitate volume fraction of the baseline material,  $GP_{EN}$  is the energy under the nugget GP zone dissolution peak, and  $GP_{EI}$  is the energy under the GP zone dissolution peak at a location in the HAZ.

Equation [1] implies that the  $\eta'/\eta$  precipitate volume fraction immediately after welding is inversely related to the area under the GP zone dissolution peak.

The precipitate weight fraction of the baseline material was calculated using ThermoCalc CALPHAD software and the COST2 database at typical aging temperatures between 394 K and 488 K (121 °C and 175 °C). The alloy composition used for the analysis was the nominal composition for 7055. The precipitate and matrix weight fractions were converted to volume fractions using standard weight fraction to volume fraction equations. This required knowledge of the precipitate and matrix densities. The density used for  $\eta$  precipitates was 5.20 g/cm<sup>3</sup>.<sup>[38]</sup> The density of the matrix was calculated using the Eq. [2] below<sup>[39]</sup>:

$$\rho = \frac{100}{\text{wt pct Al} * 0.3705 + \text{wt pct Cu} * 0.1116 + \text{wt pct Mg} * 0.5522 + \text{wt pct Zn} * 0.1401} \quad [2]$$

area under the GP zone dissolution peak in Figure 10 is within 5 pct of the area under the GP formation curve of the as-quenched scan in Figure 8. The broad width of the GP zone dissolution peak and merging of the  $\eta'$  and  $\eta$  formation peaks imply a wide distribution of GP zone radii in the nugget. The presence of a  $\eta$  coarsening peak suggests that the  $\eta$  precipitates were either formed during the DSC scan or were already present.

A quantitative estimate of the combined  $\eta'/\eta$  precipitate volume fraction immediately following friction stir welding can be made from the analysis of the GP zone dissolution peaks of the DSC scans, when combined with CALPHAD analysis. In this analysis, it is assumed that 100 pct of the GP zones detected in each DSC scan were re-precipitated during the natural aging interval after welding. These GP zones formed utilizing solute from  $\eta'/\eta$  precipitates that dissolved during welding. It is also assumed that the volume fraction of GP zones in the baseline material is insignificant. A third assumption is that the precipitate structure in the central nugget zone of the weld is 100 pct GP zone so that the GP zone dissolution peak for the nugget represents 0 pct combined  $\eta'/\eta$  precipitate volume fraction. Areas under peak II, the GP zone dissolution peak, in each DSC scan, as a function of distance from the weld center, are shown in Table II.

The precipitate volume fraction is computed using Eq. [1] below:

$$f_v = f_{vb} \left( \frac{GP_{EN} - GP_{EI}}{GP_{EN}} \right), \quad [1]$$

The calculated precipitate volume fractions varied from 0.0525 at 394 K (121 °C) to 0.0515 at 488 K (175 °C). Thus, a value of 0.052 was used as the value for  $f_{vb}$  in Eq. [1]. Two methods were used to validate the CALPHAD procedure. Small angle X-ray scattering measurements for alloy 7055 were found in the literature that yielded precipitate volume fractions between 0.052 and 0.054 when aged between 393 K and 453 K (120 °C and 180 °C) until an equilibrium precipitate volume fraction was attained.<sup>[40]</sup> The second method involved performing the same CALPHAD calculation for nominal composition aluminum alloy 7449. This resulted in an  $f_{vb}$  value of 0.054. This alloy was chosen due to its similar composition to 7055. Small angle X-ray scattering (SAXS) measurements in 7449-T79 by Dumont *et al.* revealed a baseline precipitate volume fraction between 0.053 and 0.054.<sup>[9]</sup> Thereby indicating that the  $f_{vb}$  value computed using CALPHAD for 7055 is reasonable.

The results of the precipitate volume fraction calculations as a function of position within the HAZ are shown in Figure 11. The volume fraction drops monotonically from a value of 0.052 in the baseline material to 0.044 at the location of the hardness minimum near the HAZ/TMAZ boundary. Similar precipitate volume fraction measurements using SAXS by Dumont *et al.*<sup>[9]</sup> in 7449-T79 show a slightly more complex behavior in which the precipitate volume fraction drops from a baseline value of 0.054 to 0.040 at a location corresponding to approximately 20 to 22 mm from the weld center in this study. They then observed a small increase

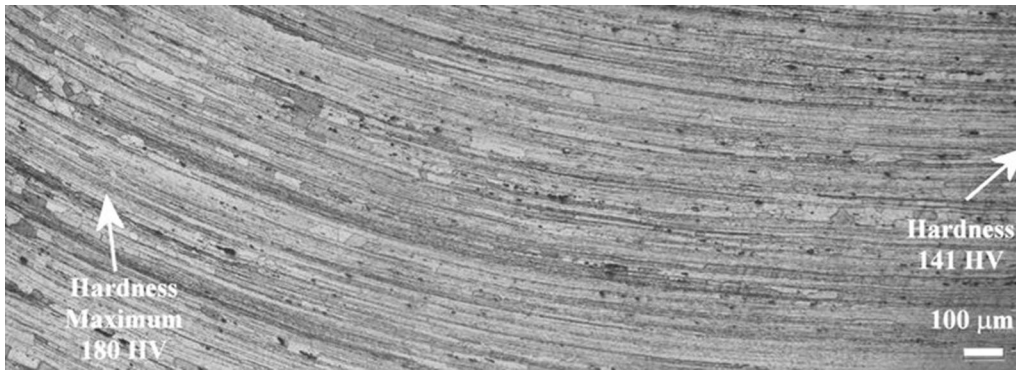


Fig. 5—Microstructure of TMAZ; 10.1 to 12.5 mm from weld center. Grains are unrecrystallized. Note rapid change in hardness in this region.

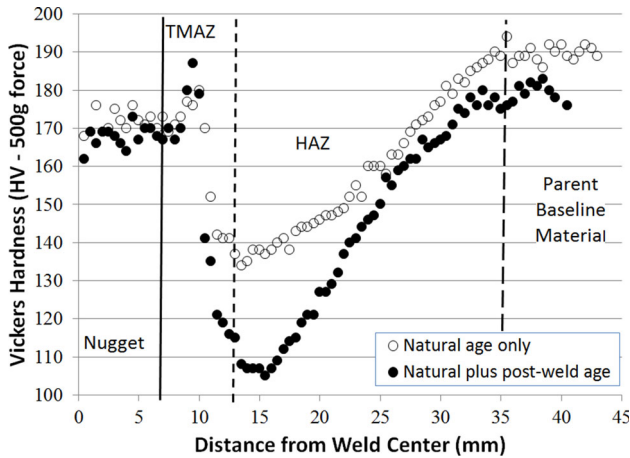


Fig. 6—Hardness profiles at mid-thickness for as-welded/naturally aged 10 years and post-weld aged.

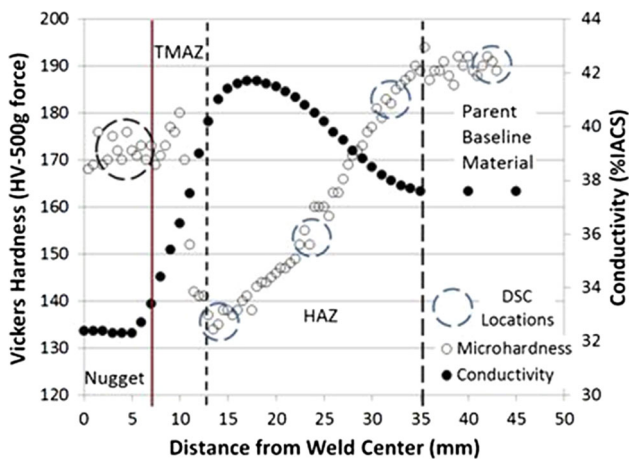


Fig. 7—Microhardness and electrical conductivity of welded and 10-year naturally aged 7055. Locations at which DSC specimens were taken are denoted *via* dashed circles.

in precipitate volume fraction to 0.044 at the hardness minimum. Thus, the results from analysis of DSC scans of 7055 friction stir welds comparable very favorably to those made *via* SAXS for 7449 friction stir welds.

DSC scans for the post-weld aged welds in the baseline and HAZ regions are shown in Figure 12. It

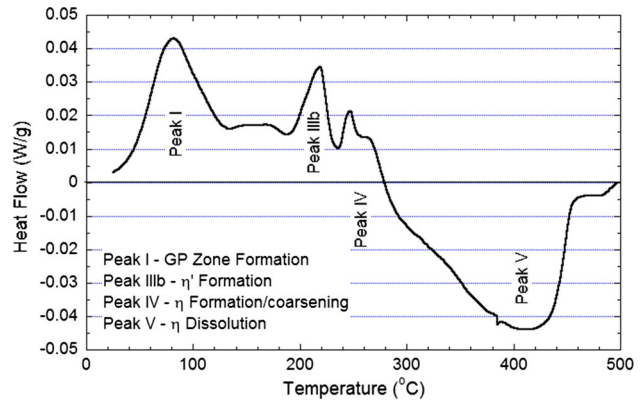


Fig. 8—DSC scan of solutionized and as-quenched 7055 showing formation peaks of GP zones,  $\eta'$  and  $\eta$  precipitates (Peaks I, IIIb, and IV). Peak V is the dissolution peak for  $\eta$ .

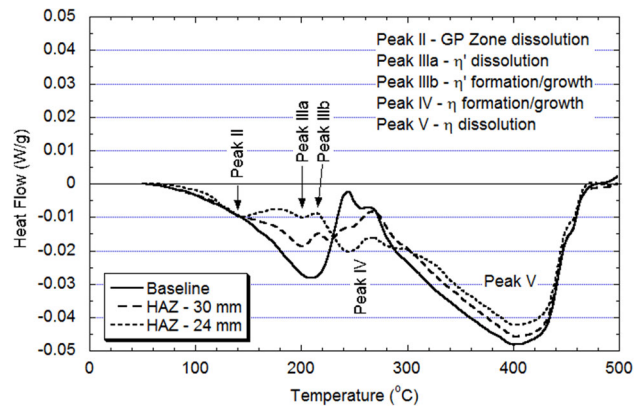


Fig. 9—DSC scans of 10-year natural-aged 7055 baseline -T77 material and specimens from two locations within the HAZ of the friction stir weld. Curves show coarsening of  $\eta'$  and  $\eta$  precipitates and evidence of increasing precipitate dissolution as the weld center is approached.

was anticipated that the post-weld aging would eliminate the GP zones observed in the as-welded material either by growth and transformation of the zones or by their dissolution and re-precipitation followed by transformation to  $\eta'$  and  $\eta$  precipitates. The post-weld aging should also increase the amount of  $\eta'$  transformation and  $\eta$  precipitate coarsening.<sup>[41]</sup> Figure 12 supports

**Table I. Precipitate Reactions Observed in 7055 DSC Scans**

Peak ID	Temperature At Peak Maximum [K (°C)]	Primary Reaction	Possible Overlapping Reactions
I	353 (80)	GP zone formation	
II	413 to 418 (140 to 145)	GP zone dissolution	$\eta'$ dissolution
IIIa	473 to 488 (200 to 215)	$\eta'$ dissolution	$\eta'$ formation/growth
IIIb	488 to 498 (215 to 225)	$\eta'$ formation/growth	$\eta'$ dissolution
IVa	513 to 523 (240 to 250)	$\eta$ formation	$\eta'$ dissolution
IVb	538 to 543 (265 to 270)	$\eta$ growth	$\eta$ dissolution
V	678 to 683 (405 to 415)	$\eta$ dissolution	

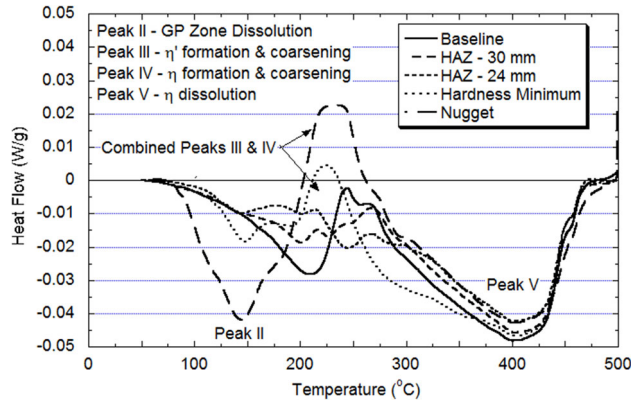


Fig. 10—DSC scans of friction stir weld natural aged for 10 years. Specimen locations span the entire width of the weld from the nugget to the baseline material.

**Table II. Energy Under GP Zone Formation or Dissolution Peaks at All Locations Tested in 7055 Friction Stir Weld Natural Aged for 10 Years**

	GP Zone Formation or Dissolution Energy (J/g)
As-quenched	9.4*
Nugget	9.0
Hardness minimum	1.4
HAZ—24 mm	0.8
HAZ—30 mm	0.2
Baseline	0

\* Formation energy.

these statements. There are no indications of GP zone dissolution peaks. The only peaks present correspond to  $\eta'$  dissolution (peak IIIa),  $\eta$  formation and coarsening (peak IV), and  $\eta$  dissolution (peak V). The initial dissolution peaks begin at a temperature corresponding to the final-step aging temperature of 438 K (165 °C), as opposed to much lower initial dissolution temperatures for the as-welded material. Comparison of the baseline curves in Figures 10 and 12 shows a decrease in the  $\eta'$  dissolution and  $\eta$  formation areas after the post-weld age. The  $\eta$  coarsening peak remains approximately constant. This is consistent with previous research<sup>[24]</sup> that shows the same effects as increasing overaging time.

As the location in the HAZ approaches the weld center, the area under Peak IIIa increases and the peak shifts to higher temperatures, the  $\eta$  formation peak

disappears, and the  $\eta$  coarsening peak diminishes. This is consistent with a precipitate microstructure in which the  $\eta'$  content is decreasing both the  $\eta'$  and  $\eta$  precipitates are coarsening and the  $\eta$  volume fraction is increasing. At the hardness minimum there are no formation or coarsening peaks. The DSC scan consists of one dissolution peak. This result indicates a precipitate structure consisting of coarse  $\eta$  phase.

The DSC scan in the nugget is similar to the as-welded baseline material with minor differences. The similarities are that the scan consists of a  $\eta'$  dissolution peak, and the  $\eta$  formation/coarsening doublet. The differences are that the dissolution peak starts at a higher temperature, possibly due to a higher final aging temperature during the T76 post-weld aging than during the T77 aging, and a larger  $\eta$  coarsening peak.

## V. DISCUSSION

The friction stir welding process imposes a short-lived, non-isothermal temperature excursion on the material in the heat-affected zone surrounding the weld. Typical welding parameters produce thermal excursions that last from 45 seconds to 2 minutes with the time spent above 473 K (200 °C) lasting 20 to 40 seconds.<sup>[10]</sup> Research performed on similar temperature excursions such as reversion, arc welding, and ramp heating have shown that the initial response of precipitates to a sudden temperature increase is dissolution of precipitates whose radius is less than the critical particle size,  $r^*$ . The amount of dissolution increases as the temperature during the thermal excursion increases with the maximum temperature attained being more important than time at temperature. In typical 7XXX aluminum alloys, GP zones dissolve between about 323 K and 423 K (50 °C and 150 °C),  $\eta'$  precipitates begin to dissolve above the final aging step temperature, but begin to rapidly dissolve above 463 K (190 °C),  $\eta$  phase precipitates between 488 K and 523 K (215 °C and 250 °C), and coarsens above 523 K (250 °C). The  $\eta$  precipitates start to dissolve above 593 K (320 °C).<sup>[11,42]</sup> During the typical 20 to 40 seconds experienced above 573 K (300 °C), it is observed that small  $\eta'$  and  $\eta$  precipitates dissolve, large  $\eta'$  precipitates transform to  $\eta$ , and larger  $\eta$  precipitates coarsen.<sup>[10,43]</sup> If the heating rate is slow enough it is possible for metastable precipitates to transform to a more stable precipitate form.<sup>[41–43]</sup> As the length of time of the thermal excursion increases, the mean precipitate size and width of the precipitate size



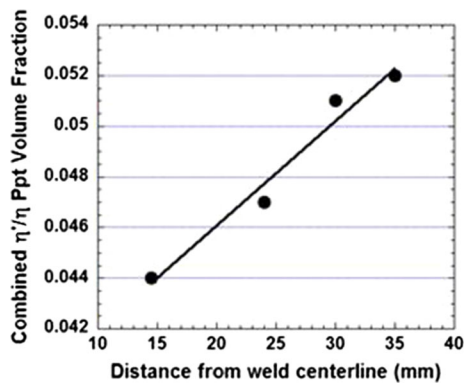


Fig. 11—Combined  $\eta'/\eta$  precipitate volume fraction as a function of location within the HAZ of a 7055 friction stir weld.

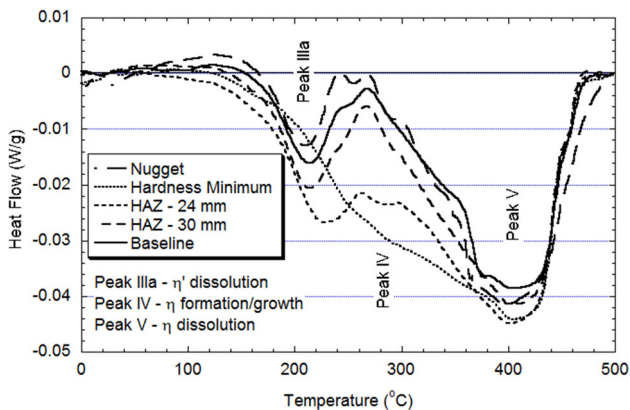


Fig. 12—DSC scans of post-weld aged friction stir weld. Specimen locations span the entire width of the weld from the nugget to the baseline material.

distribution also increase due to coarsening of the larger precipitates that survived the initial heating ramp.<sup>[43]</sup> It is typically observed that the hardness minimum occurs at the location at which the peak thermal excursion temperature is approximately 623 K (350 °C).<sup>[11]</sup> SAXS measurements in 7449 have shown that the hardness minimum occurs at the point where precipitate volume fraction has decreased by about 20 pct and the mean precipitate radius has increased by a factor of 3 or 4.<sup>[9]</sup> At locations closer to the weld center than the hardness minimum, the precipitate volume fraction, immediately after welding, drops rapidly and precipitate radius and mean spacing both increase rapidly.<sup>[9]</sup>

The contribution of precipitation to yield strength increase is dependent on the precipitate–dislocation interaction. For small shearable precipitates, such as GP zones and small  $\eta'$  precipitates, the yield strength change is given by

$$\Delta\sigma = cf^m r_p^q, \quad [3]$$

where  $f$  is the precipitate volume fraction,  $r_p$  is the mean precipitate diameter, and the exponents  $m$  and  $q$  are generally around 0.5. Dislocations loop around precipitates that are too large to be sheared, such as  $\eta$

precipitates and larger  $\eta'$  precipitates. For this case of Orowan strengthening the yield strength change is given by

$$\Delta\sigma = \beta r_p^{-1} f^{0.5} \quad [4]$$

Since the parent material is overaged, Eq. [4] is primarily applicable in the HAZ. Eq. [3] is applicable in the nugget and a combination of the two equations is applicable in the TMAZ. Both equations show that strength increases with the square root of precipitate volume fraction.

Electrical conductivity in heat-treatable aluminum alloys is a function of solute content in the matrix and precipitate spacing. The spacing is itself a function of the amount and type of precipitates present. Electrical conductivity increases as matrix solute content decreases (or precipitate volume fraction increases) and precipitate spacing increases.<sup>[44]</sup> The largest conductivity values are associated with alloys in the annealed condition which are characterized by large, widely spaced precipitates in a matrix largely depleted of solute. The lowest values of conductivity are associated with alloys that have been naturally aged for several days. In this condition the matrix has a significant solute content while the precipitate structure consists of closely spaced GP zones. During artificial aging, at temperatures typically used for 7XXX alloys, the conductivity at first remains constant with increasing time and then increases as the GP zones gradually transform to  $\eta'$  and  $\eta$ , the precipitate spacing increases, and the matrix is increasingly depleted of solute.

#### A. Naturally Aged Material

The results of all three characterization techniques can be combined to interpret the precipitate evolution during welding and subsequent natural and artificial aging. After the 10-year natural age in the nugget all three characterization techniques provide ample evidence that the precipitate structure is composed of GP zones. The hardness has recovered to about 90 pct of the baseline, the conductivity is significantly less than the baseline, and the GP zone dissolution peak in the DSC scan has an area virtually identical to the GP zone formation area of the as-quenched material. These results agree well with those in presented by Kalembe *et al.* for a naturally aged 7136 friction stir weld.<sup>[14]</sup>

Likewise, at the hardness minimum found at the TMAZ/HAZ interface, the conductivity is near its maximum. The accompanying DSC scan shows no evidence of  $\eta$  precipitate formation or coarsening, but does show small GP zone dissolution and  $\eta'$  formation/broadening peaks. These results are consistent with a stable, coarse, widely spaced distribution of  $\eta$  precipitates. The GP zones being the result of re-precipitation after precipitate dissolution during welding.

In the HAZ, the microhardness increases and conductivity decreases as distance from the weld center increases. The DSC scans exhibit decreasing GP zone dissolution areas, increasing  $\eta'$  formation areas, and

increasing  $\eta$  formation/coarsening peak areas. All these results are consistent with a reduction in the maximum temperature attained during welding as the distance from the weld center increased. The lower the temperature excursion during welding, the less precipitate dissolution that leads to GP zone formation and the lower amount of precipitate coarsening.

All of the results discussed to this point are qualitative in nature and can be anticipated from previous work in the literature. The unique aspect of this study is the quantitative measurement of  $\eta'/\eta$  precipitate totals through the combination of DSC and CALPHAD analysis. The results of this study agree remarkably well with a similar study that used a much more expensive SAXS characterization technique which is available at many fewer lab facilities.<sup>[9]</sup> The analysis in the current study focused on analysis of the GP zone dissolution peak. However, due to multiple and simultaneous precipitate reactions occurring at temperatures corresponding to  $\eta'$  and  $\eta$  precipitate transformations, it is difficult to quantitatively separate the amounts of those precipitate types using the DSC/CALPHAD methodology.

### B. Post-weld Aged Material

As discussed in the section IV, the DSC scan from the nugget region of the post-weld aged material is very similar to the naturally aged baseline -T77 material. The microhardness results are virtually identical to those for the natural aged material. This result is fortuitous, as the precipitate structures of the two conditions are very different. What is more important is that the nugget hardness in the post-weld aged nugget is very close to that of the overaged parent material. The results suggest that the post-weld aging transformed the GP zones in the naturally aged nugget to more stable precipitates characteristic of an overaged temper. The smaller GP zones likely re-dissolved and re-precipitated, whereas the larger GP zones simply transformed directly to  $\eta'$ . The post-weld aged baseline DSC scan and hardness are consistent with that observed with continued overaging of a -T77 temper. That is, a decrease in hardness and a shift of the DSC  $\eta$  formation peak to the  $\eta$  broadening peak, as may be observed by comparing the baseline peaks in Figures 10 and 12.

The greatest drop in hardness due to the post-weld aging occurred at the TMAZ/HAZ boundary. This is consistent with other authors that have studied effects of natural aging.<sup>[14,45]</sup> The difference in hardness is due to transformation of the GP zones to more stable, coarse, widely spaced precipitates during aging. This is supported by the DSC scan showing only a broad dissolution peak.

The microhardness difference between the naturally aged and post-weld aged material decreases from a maximum at the TMAZ/HAZ interface to a difference of about 10 HV at 24 mm from the weld center. At greater distances the hardness difference remains constant. This suggests that between 15 and 24 mm from the weld center that the primary cause of the hardness difference is due to GP zone dissolution/transformation during post-weld aging. However, there are no DSC

scans between these two positions to confirm the suggestion. Comparison of DSC scans at distances 24 mm and greater in Figures 10 and 12 clearly indicate lack of  $\eta'$  formation peaks in post-weld aged material and similar coarsening peaks in both materials. This together with very small GP zone dissolution peaks in the naturally aged material supports the coarsening of precipitates as the primary effect of post-weld aging on precipitate microstructure and the lack of a significant contribution of GP zones to hardness.

## VI. CONCLUSIONS

The combination of differential scanning calorimetry, microhardness, electrical conductivity, and optical metallography was successfully used to both qualitatively and semi-quantitatively characterize the micro- and precipitate structure of a 7055 friction stir weld.

The characterization effort was able to confirm that precipitates in the heat-affected zone (HAZ) undergo a mixture of dissolution and coarsening during welding, the extent of which increases as the location approaches the weld center.

At the hardness minimum (TMAZ/HAZ interface) the precipitates are stable, coarse, and widely spaced  $\eta$  phase. The precipitate volume fraction was calculated to have decreased by 15 pct at this point as compared to the baseline material.

In the nugget, the precipitate structure was composed of GP zones that precipitated during the 10-year natural aging period.

A -T76-type post-weld age resulted in the transformation of GP zones to  $\eta'$  and  $\eta$  precipitates and coarsening of the metastable and equilibrium  $\eta'$  and  $\eta$  precipitate phases.

The characterization effort in combination with CALPHAD calculations enabled calculation of  $\eta'/\eta$  precipitate volume fraction as a function of position within the HAZ.

## ACKNOWLEDGMENTS

The authors acknowledge donation of the material used for this work from the Alcoa Inc. Sheet and Plate Division in Davenport, IA. They would also like to acknowledge the research group of Dr. Anthony Reynolds at the University of South Carolina for friction stir welding the 7055 plate. The assistance of Mr. Joe Royall and Dr. Sandeep Shah for machining DSC specimen cylinders and setting up electrical conductivity measurement was appreciated.

## REFERENCES

1. W.M. Thomas, E.D. Nicholas, J.C. Needham, M.G. Murch, P. Temple-Smith, and C.J. Dawes: GB Patent no. 9125978-8, 1991.
2. W.M. Thomas, E.D. Nicolas, J.C. Needham, M.G. Murch, P. Temple-Smith, and C.J. Dawes: US Patent no. 5 460 317; EPS 0 616 490, 1991.

3. C.E. Cross, D.L. Olson, and S. Liu: *Handbook of Aluminum. Physical Metallurgy and Processes*, Marcel Dekker, New York, 2003, vol. 1, pp. 481–532.
4. P.L. Threadgill, A.J. Leonard, H.R. Shercliff, and P.J. Withers: *Int. Mat. Rev.*, 2009, vol. 54, pp. 49–93.
5. J.C. Ehrström, A. Bigot, L. Cervi, and H. Gérard, AeroMat 2003.
6. B.M. Tweedy, C.A. Widener, and D.A. Burford: 6th *International Symposium on Friction Stir Welding Saint-Sauveur*, Nr Montréal, Canada, October 10–13, 2006, paper 37.
7. C.B. Fuller, M.W. Mahoney, M. Calabrese, and L. Miconi: *Mater. Sci. Eng. A*, 2010, vol. 527, pp. 2233–40.
8. D.P.P. Booth, M.J. Starink, and I. Sinclair: *Mater. Sci. Technol.*, 2007, vol. 23, pp. 276–84.
9. M. Dumont, A. Steuwer, A. Deschamps, M. Peel, and P.J. Withers: *Acta Mater.*, 2006, vol. 54, pp. 4793–801.
10. N. Kamp, A.P. Reynolds, and J.D. Robson: *Sci. Technol. Weld. Joining*, 2009, vol. 14, pp. 589–96.
11. A.P. Reynolds, W. Tang, Z. Khandar, J.A. Khan, and K. Lindner: *Sci. Technol. Weld. Joining*, 2005, vol. 10, pp. 190–99.
12. P. Upadhyay and A.P. Reynolds: *Mater. Sci. Eng. A*, 2010, vol. 527, pp. 1537–43.
13. J.D. Robson, P. Upadhyay, and A.P. Reynolds: *Sci. Technol. Weld. Join.*, 2010, vol. 15, pp. 613–18.
14. I. Kalembe, C. Hamilton, and S. Dymek: *Mater. Des.*, 2014, vol. 60, pp. 295–301.
15. A.P. Reynolds, W.D. Lockwood, and T.U. Seidel: *Mater. Sci. Forum*, 2000, vols. 331–337, pp. 1719–24.
16. M.W. Mahoney, C.G. Rhodes, J.G. Flintoff, R.A. Spurling, and W.H. Bingel: *Metall. Mater. Trans. A*, 1998, vol. 29A, pp. 1955–64.
17. M. Strangewood, J.E. Berry, D.P. Cleugh, A.J. Leonard, and P.L. Threadgill: *Proc. 1<sup>st</sup> Int. Symp. on 'Friction stir welding'*, Thousand Oaks CA, USA, June 1999, TWI.
18. K.V. Jata, K.K. Sankaran, and J.J. Ruschau: *Metall. Mater. Trans. A*, 2000, vol. 31A, pp. 2181–92.
19. C. Genevois, A. Deschamps, A. Denquin, and B. Doisneaucottignies: *Acta Mater.*, 2005, vol. 53, pp. 2447–58.
20. A. Sullivan and J.D. Robson: *Mater. Sci. Eng. A*, 2008, vol. A478, pp. 351–60.
21. L.E. Svensson, L. Karlsson, H. Larsson, B. Karlsson, M. Fazzini, and J. Karlsson: *Sci. Technol. Weld. Join.*, 2000, vol. 5, pp. 285–96.
22. J. Buha, R.N. Lumley, and A.G. Crosky: *Mater. Sci. Eng. A*, 2010, vol. 492, pp. 1–10.
23. X. Li and M.J. Starink: *Mater. Sci. Forum*, 2000, vols. 331–337, pp. 1071–76.
24. X.M. Li and M.J. Starink: *J. Mater. Eng. Perform.*, 2012, vol. 21, pp. 977–84.
25. N. Kamp, I. Sinclair, and M.J. Starink: *Metall. Mater. Trans. A*, 2002, vol. 33A, pp. 1125–36.
26. M.J. Starink and S.C. Wang: *Acta Mater.*, 2003, vol. 51, pp. 5131–50.
27. M.J. Starink: *Int. Mater. Rev.*, 2004, vol. 49, pp. 191–226.
28. R. Dorward: *Mater. Sci. Technol.*, 1999, vol. 15, pp. 1133–38.
29. T. Marlaud, A. Deschamps, F. Bley, W. Lefebvre, and B. Baroux: *Acta Mater.*, 2010, vol. 58, pp. 248–60.
30. R. Delasi and P.N. Adler: *Metall. Trans. A*, 1977, vol. 8A, pp. 1177–83.
31. P.N. Adler and R. DeFasi: *Metall. Trans. A*, 1977, vol. 8A, pp. 1185–90.
32. J.K. Park and A.J. Ardell: *Mater. Sci. Eng. A*, 1989, vol. 114, pp. 197–203.
33. E.S. Tankins and W.E. Frazier: *Mater. Perform.*, 1987, vol. 26, pp. 37–44.
34. J.M. Papazian: *Metall. Trans. A*, 1982, vol. 13A, pp. 761–69.
35. X.J. Wu, A.K. Koul, and L. Zhao: *Can. Aeronaut. Space J.*, 1996, vol. 42, pp. 93–101.
36. A. Yamamoto, K. Minami, U. Ishihara, and H. Tsubakino: *Mater. Trans. JIM*, 1998, vol. 39, pp. 69–74.
37. J.M. Papazian: *Mater. Sci. Eng.*, 1986, vol. 79, pp. 97–104.
38. J.E. Hatch: *Aluminum: Properties and Physical Metallurgy*, American Society for Metals, Metals Park, 1984, p. 31.
39. Aluminum Standards and Data 1990, 10th edition, the Aluminum Association, Washington, DC, 1990, pp. 41–42.
40. Z. Du, T. Zhou, P. Liu, H. Li, B. Dong, and C. Chen: *J. Mater. Sci. Technol.*, 2005, vol. 21, pp. 479–83.
41. M. Nicolas and A. Deschamps: *Mater. Sci. Forum*, 2002, vols. 396–402, pp. 1561–66.
42. M. Nicolas and A. Deschamps: *Acta Mater.*, 2003, vol. 51, pp. 6077–94.
43. T. Marlaud, A. Deschamps, F. Bley, W. Lefebvre, and B. Baroux: *Acta Mater.*, 2010, vol. 48, pp. 4814–26.
44. M.A. Salazar-Guapuriche, Y.Y. Zhao, A. Pitman, and A. Greene: *Mater. Sci. Forum*, 2006, vols. 519–521, pp. 853–58.
45. A.J. Leonard: *Proc. 2nd Int. Symposium on 'Friction stir welding'*, Gothenburg, Sweden, June 2000.